Research Article | Vol. 27, No. 4 | 18 Feb 2019 | OPTICS EXPRESS 4386
Optics EXPRESS

Modal instabilities in high power fiber laser oscillators

V. SCARNERA,[1,2,*] F. GHIRINGHELLI,[1] A. MALINOWSKI,[1] C. A. CODEMARD,[1] M. K. DURKIN,[1] AND M. N. ZERVAS[1,2]

[1]SPI Lasers, Wellington Park, Toolbar Way, Hedge End, SO30 2QU, Southampton, UK
[2]Optoelectronics Research Centre, University of Southampton, Highfield, SO17 1BJ, Southampton, UK
[*]v.scarnera@soton.ac.uk

Abstract: Transverse mode competition and instabilities in high-power fiber oscillators have been studied experimentally by monitoring the dynamic power exchanges and characteristic frequencies of the transmitted fundamental mode (FM) and scattered high-order modes (HOMs) of the fiber laser cavity under CW and pulsed pumping. The FM and HOM power evolution indicates the presence of two competing effective laser cavities which result in rich output dynamics and full chaotic operation. The thermal and inversion related contributions to the observed instabilities have been identified by monitoring the associated characteristic instability frequencies under pulsed pumping. It is shown that in the transient regime, both inversion and thermal effects contribute successively to the observed power instabilities. Increasing the pump power leads to full chaotic response through an interplay between transverse and longitudinal mode instabilities.

1. Introduction

Transverse mode instability (TMI) is a recently observed nonlinearity [1] proving to be a major power-scaling limitation in high-power fiber lasers and amplifiers [2–4]. It amounts to a sudden output beam break-up and beam-quality degradation above an output power threshold [1]. TMI is widely attributed to a refractive index (RI) grating formation due to transverse mode beating and coupling between the amplified fundamental mode (FM) and high order modes (HOM). In high power operation, the RI grating has been considered to be induced by thermo-optic effects [4–13]. At low powers and high gain conditions, on the other hand, TMI has been attributed predominantly to inversion related RI changes [16,17]. In a recent work and in clear departure from previous approaches, a stability analysis in the presence of thermal and inversion-related RI changes has been performed, showing that the amplification process of the FM in multimode fibers is fundamentally unstable above a signal power threshold [19,20]. In this context, TMI can be viewed as the spatial counterpart to the well-known temporal modulation instability (MI) widely observed in nonlinear single-mode passive fibers [21] or amplifiers and lasers [22].

So far, the majority of TMI theoretical and experimental investigations deal with high power fiber amplifiers in master-oscillator power amplifier (MOPA) configurations [4–18], and only a small numbers of recent reports deal with TMI in single-cavity high-power fiber laser (HPFL) oscillators [23–26]. The TMI power threshold has been shown to reduce in the presence of back reflections in amplifiers [17,27–29], and, therefore, TMI effects are expected to be more pronounced and complex in HPFL oscillators than in amplifiers.

In addition to TMI power threshold, which is shown to be inversely proportional to the fiber core diameter [1–3,19,20], another important parameter in the study of TMI is the associated frequency, which is related to the characteristic time scale of the dominant physical mechanism responsible for the instability. It has been experimentally observed that the

#345380 https://doi.org/10.1364/OE.27.004386
Journal © 2019 Received 13 Sep 2018; revised 8 Nov 2018; accepted 17 Nov 2018; published 7 Feb 2019

Optics EXPRESS

characteristic TMI frequencies in high power fiber amplifiers varies in the 0.2-5kHz range, as the fiber core diameter varies from 100μm to 20μm, and again it is generally inversely proportional to fiber core area [8,14,15]. This dependence is closely related to the thermal diffusion time across the fiber core [7,8], and clearly demonstrates the dominance of thermal effects in high power fiber amplifiers TMI. In low-power (2W −12W), small-core-diameter (~10μm) fiber amplifiers, on the other hand, the TMI frequency has been experimentally shown to vary linearly with the signal output power [29], in close agreement with the inversion-related dependence [7]. It should be stressed that in this case dominance of thermal effects would have resulted in TMI frequencies largely independent of the signal power.

So far, most of the experimental TMI work has been carried out under steady-state pumping conditions and, as a consequence, the transient response and TMI build-up is to some extend overlooked [30–32]. Transient effects are extremely important, as they provide useful additional information regarding the time dependence of the various contributions to the overall instability [16].

In reports dealing with TMI in fiber amplifiers, where the output fiber facet is accessible, high-speed cameras and/or fast photo-detectors are utilized and TMI is explicitly observed in the spatial and time domain, respectively [8]. Conversely, in the reports dealing with TMI in HPFL oscillators [23–26], evidence of TMI has been inferred by simply measuring the laser output power dynamics, without explicit evidence of inter-modal power exchange and competition. Gratings formation due to inversion related effects have been measured and theoretically modelled in low power fiber amplifiers [16], however, to our knowledge, inversion related gratings have never been reported in HPFLs.

In this paper, we characterize transverse modal competition and instabilities in HPFL oscillators, identifying both thermal-related and inversion-related effects. In Section 2, the experimental part describes the measurement scheme adopted, and the composite laser cavity under test. Section 3 describes the experimental results obtained under CW and pulsed pumping scenarios. Both time and frequency resolved measurements are presented. The characteristic frequencies, under transient response, are utilized to identify the relative contribution of thermal and inversion-related effects. Three different instability zones are described, as the pump power increases, leading to full chaotic response. Section 4 summarizes the main results. In Appendix A, the characteristic timescales of thermal and inversion related transients in active fibers are derived.

2. Experimental setup

The fiber laser scheme and experimental setup are illustrated in Fig. 1. The active fiber of the laser under test is a multimode (MM) Yb^{3+}-doped SPI Lasers GTWave [33,34] with core radius of ~8μm and V number of ~4. Active fiber length is 21m, with absorption at 950nm equal to 0.85dB/m. The effective index of refraction of the fundamental mode is 1.45. The two ends of the active fiber are spliced to matched single-mode (SM) fiber pigtails with high reflector (HR) and output coupler (OC) fiber Bragg gratings, centered at 1070nm and written directly in their cores. OC reflectivity is 15% and HR reflectivity is >99%. The length of the pigtail, from the MM active fiber's splice to the gratings is 1m for each grating. Gratings' fibers have a core radius of 6um and a numerical aperture equal to 0.05.

In addition, the OC fiber pigtail incorporates a cladding mode stripper (CMS). CMS removes the unwanted light coupled and guided in the cladding of the passive fibers. Light stripping from the passive fiber cladding is obtained by using a section of coating having higher index of refraction than that of fiber's cladding. Apart from in the CMS section (10cm long), everywhere else in the laser, fiber coating has lower index than the cladding.

Optical fibers and gratings are attached on a water-cooled heat sink maintained at 20°C. The outputs of the HR and OC pigtail are terminated by an angle-cleaved 50μm core fiber and 11m long 50μm core fiber, respectively, in order to minimize back-reflections into the fiber oscillator. The intra-cavity CMS is used to strip-off any remnant pump power, as well as,

Optics EXPRESS

signal power scattered into the cladding at the OC pigtail splice. It should be mentioned that the signal power stripped by the CMS is primarily due to scattering of signal HOM at the MM/SM output splice. The fiber length between the CMS and output is 8m corresponding to 40ns optical delay.

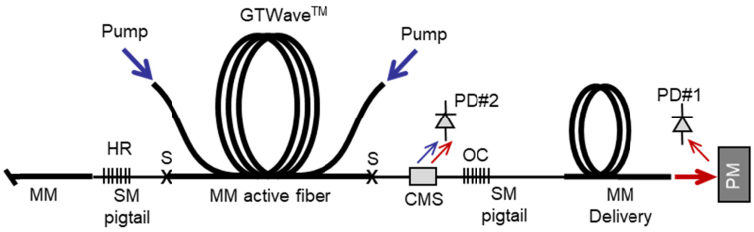

Fig. 1. Fiber laser scheme and experimental setup.

The system is pumped by combined 950nm diodes from both sides of the GTWave in CW regime or with square pump pulses (1 kHz, 20% Duty Cycle). The output power of the system is measured with a thermal head. Two photodiodes PD#1 and PD#2, connected to an 8GHz oscilloscope, monitor the laser output, scattered off the thermal head power meter (PM), and the relative HOM content stripped-off by the CMS, respectively. The two PDs and their BNC cables were identical, thus providing identical electrical delays.

2.1 Effective double-cavity configuration

In HPFL oscillators and amplifiers, increasing the core's area of the active fibre mitigates nonlinear effects such as Stimulated Raman Scattering (SRS) [2]; especially since the active fibre is often the longest part. As a result, the majority of practical HPFL implementations make use of MM active fibres, which renders them prone to TMI [2–4]. To ensure near-diffraction-limited laser output, the multimode active fibre is spliced to SM pigtails. However, this spatial filtering is not ideal and small amounts of HOMs are likely to be excited. Conversely, in a reciprocal manner, HOM can couple back to the FM of the SM fibres at the two SM-to-MM splices. Such modal cross-couplings at the SM/MM splices can potentially further complicate the HPFL performance. In anticipation of the rich experimental results presented in the following sections, we propose the following possible effective double-cavity configuration.

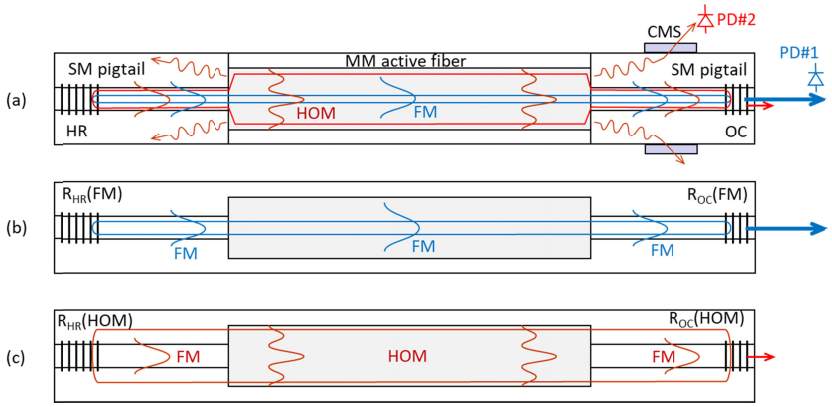

Fig. 2. Effective double-cavity fiber laser configuration; (a) possible FM/FM/FM and FM/HOM/FM closed paths in the composite SM/MM/SM fiber cavity, (b) fundamental mode cavity (FMC), (c) effective higher-order-mode cavity (HOMC).

Figure 2(a) shows a schematic of the SM/MM/SM fiber laser composite cavity, used in the experiments. The "in-coming" (with respect to the MM active fiber) FM of the SM

Optics EXPRESS

pigtail, in addition to the well-matched FM, excites small amounts of HOM of the MM active fiber. In a reciprocal manner, "out-going" HOMs can couple back partially into the FM of the SM-pigtail. This way, after reflecting back from the OC and HR gratings, two distinct FM/FM/FM and FM/HOM/FM closed paths can potentially form. Figures 2(b) and 2(c) show the FM cavity (FMC) and HOM cavity (HOMC), formed by the FM/FM/FM and FM/HOM/FM closed paths, respectively. It should be stressed that the effective reflectivities $R_{HR(HOM)}$ and $R_{OC(HOM)}$ of the HOMC are evidently much smaller than the corresponding values $R_{HR(FM)}$ and $R_{OC(FM)}$ of the FMC. As a result, a much higher roundtrip gain is required around the FM/HOM/FM closed path for the HOMC to lase or otherwise compete with the FMC lasing. It should be emphasized that the HOMC light scattered at the MM/SM splices will propagate into the cladding of the SM pigtail and it will eventually be stripped-off by CMS. Referring to the experimental setup of Fig. 1 and the schematic of Fig. 2(a), the readings of the CMS photodiode (PD#2) will, therefore, be primarily associated with HOMs of the active fiber and the activity of the HOMC. The readings of the output photodiode (PD#1), on the other hand, are associated with the FM of the active fiber and the activity of the FMC.

3. Experimental results

In this section we present the main experimental results. Two pumping modes of operation were considered, namely continuous wave (CW) and pulsed-pump mode of operation. In the CW pump mode operation (section 3.1) the oscilloscope impedance was set to high and therefore the measurement bandwidth was low. In the pulsed pump mode operation (section 3.2), on the other hand, the oscilloscope impedance was set to low and therefore high bandwidth (in 4GHz range) measurements were possible. In the CW pump mode the quoted pump power is the average power, while in the pulsed pump mode it is the peak pump power.

3.1 CW Pump mode of operation

The output power of the laser was brought up to 1600W in eight steps; each step lasted 90 seconds to allow for thermal transients to equalize. PD#1, PD#2 and thermal head readings were recorded at 2Hz (180 samples per step). The response of the thermal head was ~1sec, and the photodiode voltages were acquired with high impedance. Once averaged on the scope, photodiode readings have an effective bandwidth of 10Hz.

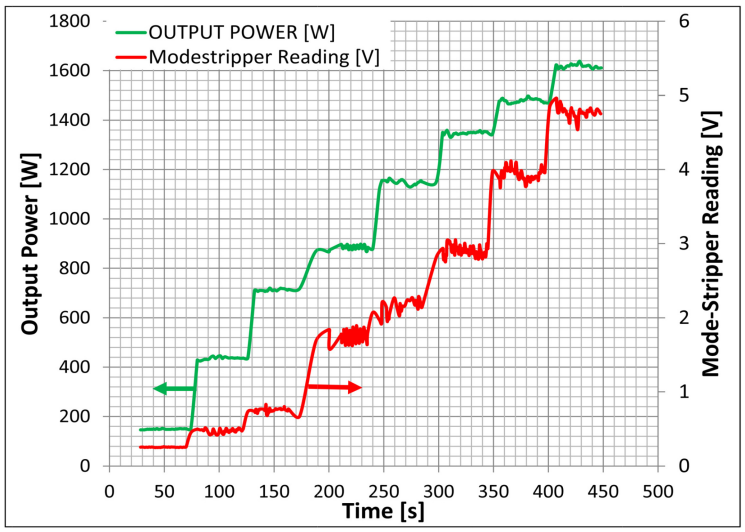

Fig. 3. CW ramp logging; in green the output power and in red the CMS photodiode reading.

Optics EXPRESS

Figure 3 shows the thermal-head power meter and the associated CMS photodiode (PD#2) readings during the pump ramp up. It is shown that the signal output and the CMS reading are concurrently unstable at any power level. Figures 4 shows the time evolution of the normalized readings of PD#1 and PD#2, at average signal output powers of (a) 438W (step#2), (b) 885W (step#4), (c) 1480W (step#7) and (d) 1620W (step#8), respectively. It is clearly shown that the two readings are in anti-phase. Since PD#1 and PD#2 readings monitor essentially the FMC and HOMC powers, it can be deduced that the two effective cavities are indeed competing. As discussed in Section 2.1, the two effective cavities overlap over the MM active fiber through the supported FM and HOM and, therefore, their power exchange is expected to be a result of transverse mode competition (TMC).

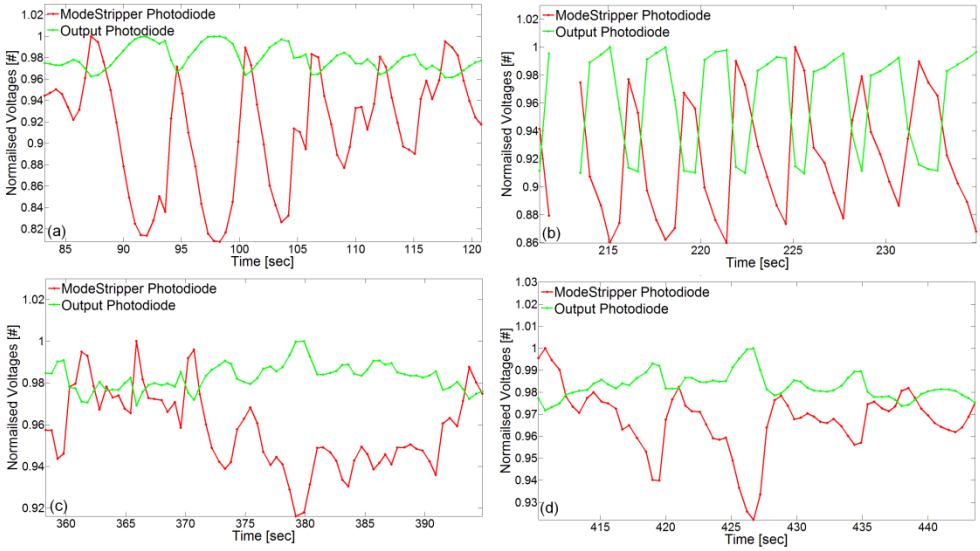

Fig. 4. Normalised readings versus time of PD#1 and PD#2 at average signal output power of (a) 438W, (b) 885W, (c) 1480W, and (d) 1620W.

The average values (over 180 samples) of the signal output power and PD#2 readings, obtained during each step of the pump ramp, are plotted against the pump power in Fig. 5. It is noticed that the slope efficiency of the laser decreases as the pump power is increased. Three distinct pump power ranges are identified, denoted as zone#1 (0-1.2kW), zone#2 (1.2-2.4kW) and zone#3 (2.4-3.5kW), where the slope efficiency changes from 62% to 51% and 38%, respectively. Conversely, PD#2 voltage slopes increase over the three zones. This clearly demonstrates that the drop in laser efficiency with pump power is due to an increasingly larger power exchange between FM and HOM in the active fiber, as a result of TMC.

Optics EXPRESS

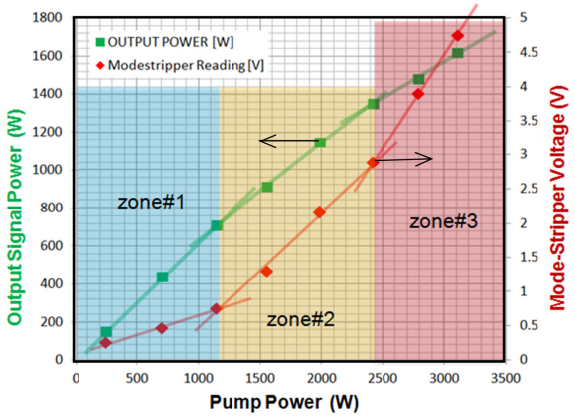

Fig. 5. Average values of the signal output power and PD#2 voltage, obtained during each step of the pump ramp, against pump power.

3.2 Pulsed pump mode of operation

In this pumping mode of operation, the semiconductor laser pumps were turned periodically on-off with square pulses. The repetition rate and duty cycle were fixed at 1 kHz and 20%, respectively, whilst the pump power was step-wise increased to its maximum level. The output and CMS pulses were recorded at all power levels. The acquisition scheme was primarily limited in bandwidth by the photodiodes (~2 GHz). Pulses detected from the output (PD#1) and from the CMS (PD#2) photodiodes are shown in Figs. 6, 7, 8 and 11, where part (a) zooms around the relaxation oscillation, part (b) shows the entire pulses normalized to their peaks, and part (c) is radio frequency (RF) spectrum (obtained from the Fourier transform of the output pulses) calculated between 20 and 200μs only, thus excluding the relaxation oscillation. In part (c), the chart grid is aligned with the free spectral range (FSR) of the laser cavity. Peaks falling at multiples of 4.48 MHz are generated by the longitudinal mode beating (LMB). Zooming into the first relaxation oscillation peaks provides information about the relative state and inversion of the two effective cavities. Monitoring the "plateau" behavior provides information about the transverse mode power exchange and competition, while the RF spectrum provides additional information about TMC, as well as, longitudinal mode competition (LMC).

3.2.1 Instability zone#1

Figure 6 illustrates the results obtained at a pump power of 486W. In Fig. 6(a) and 6(b), the relaxation oscillation overshoots and "plateau" levels of both output and CMS photodiode readings follow closely each other. The CMS (PD#2) reading appears to precede the output (PD#1) reading by 40ns, which is merely due to the 8m fiber length between the CMS and output. This implies that, in this case, the CMS power is primarily due to residual scattering of the FM at the MM/SM fiber splice. At this point there is no evidence of strong secondary cavity activity. The noisy appearance of the CMS reading (red line) is due to low-level of optical signal, dominated by electrical noise. The RF spectrum in Fig. 6(c) shows no discrete peaks or other pronounced spectral features.

Optics EXPRESS

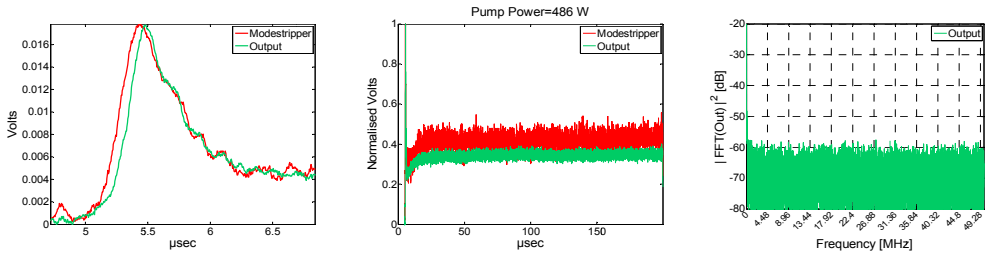

Fig. 6. Output power (PD#1-green) and CMS (PD#2-red) readings over (a) relaxation oscillation (first 6.8μs), (b), entire pump pulse duration (0-200μs), and (c) FFT of output trace over 20-200μs period. The pump power is 486W.

After the initial adjustment, the electrical gain settings of PD#1 and PD#2 were left unchanged so that absolute changes in the FM and HOM power levels were monitored and recorded. Figures 7 illustrates the results obtained at a pump power of 778W (midway in zone#1). In Fig. 7(a), we observe that the relaxation oscillations recorded at the output (PD#1-green) and CMS (PD#2-red) differ significantly, with the CMS overshoot being ~x2 higher than the output one. At this power, the CMS overshoot is actually delayed by about 56ns compared to the output peak. To calculate the true delay, the 40ns optical delay shown in Fig. 6(a) must be added to the one shown in Fig. 7(a). The temporal delay and higher overshoot recorded by PD#2 implies the presence of a HOMC, as shown schematically in Fig. 2. The HOMC has lower Q factor and, therefore, requires higher inversion than the dominant FMC. As a result, HOMC has a longer turn-on delay and higher overshoot than FMC. Figure 7(b) shows that, after ~80μsec, the two cavities start to compete indicating strong TMC. The two traces are in an anti-phase and vary periodically with a period of ~20μs and a corresponding TMC frequency of ~50 kHz. As shown in Appendix A Fig. 15, these timescales are in good agreement with the thermal diffusion time associated with 7-8μm core radius. Such thermally-induced, low-frequency component does not appear in Fig. 7(c). It should be mentioned that similar temporal behavior and low frequency, thermally-induced spectral characteristics were observed with higher pump powers within zone#1.

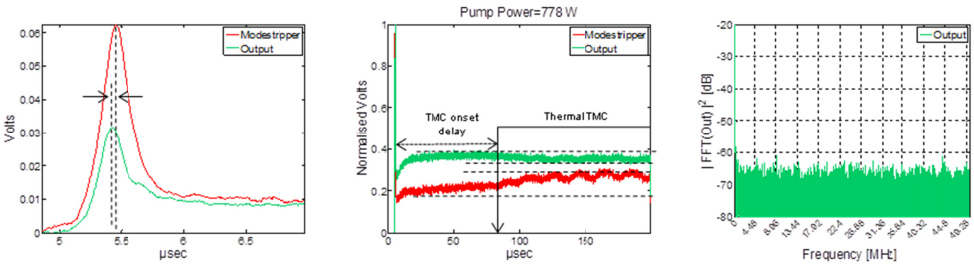

Fig. 7. Output power (PD#1-green) and CMS (PD#2-red) readings over (a) relaxation oscillation (first 6.8μs), (b), entire pump pulse duration (0-200μs), and (c) FFT of output trace over 20-200μs period. The pump power is 778W.

3.2.2 Instability zone#2

Instability zone#2 is characterized by a decrease in output power slope and an associated increase in the slope of HOM reading (PD#2), which indicates a stronger power exchange between FMC and HOMC. Figure 8 shows the results obtained with a pump power of 1497W. In Fig. 8(a), the HOMC overshoot has increased to ~x3 the FMC one. The fluctuations in the output power following the initial overshoot are likely to be due to the onset of backward SRS, which is known to destabilize the FMC [2]. As before, Fig. 8(b) shows that after a delay of ~95μs pronounced TMC takes place with the same as before frequency of ~50kHz, characteristic of a thermally-induced perturbation. However, within zone#2, soon after the first relaxation oscillation, between ~10μs and ~90μs much faster

Optics EXPRESS

dynamics were observed. In Fig. 8(c), the FFT output trace, in addition to noticeable increased cavity FSR peaks at multiples of 4.48MHz, shows strong additional peaks at ~3.05MHz (with overtone at 6.1MHz), corresponding to the observed fast TMC dynamics. From Fig. 18(b) in Appendix A, it is deduced that this range of characteristic frequencies corresponds to upper-state population (inversion) dynamics (denoted as i-TMC). The increased FSR peaks imply that TMC enhances the cavity LMB.

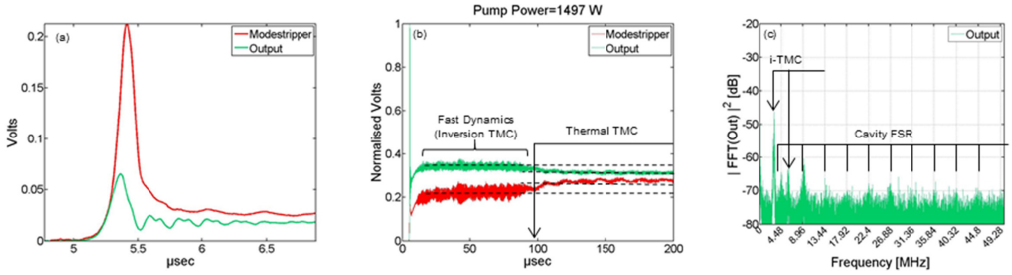

Fig. 8. Output power (PD#1-green) and CMS (PD#2-red) readings over (a) relaxation oscillation (first 6.8μs), (b), entire pump pulse duration (0-200μs), and (c) FFT of output trace over 20-200μs period. The pump power is 1497W.

Figure 9(a) shows the output power (PD#1-green) and HOM (PD#2-red) traces at a pump power of 1730W. Figure 9(b) is a zoom in the fast dynamics of Fig. 9(a) between 95 and 100μs. Clearly HOMC and FMC are in anti-phase, with oscillations in the microsecond regime, indicating fast TMC. As shown in Appendix A, the observed fast dynamics are again in good agreement with the expected population inversion relaxation time scales. The inversion-related fast dynamics are again interrupted and followed by much slower dynamics (period of ~20μs) of thermal origin. Figure 9(c) shows the corresponding FFT.

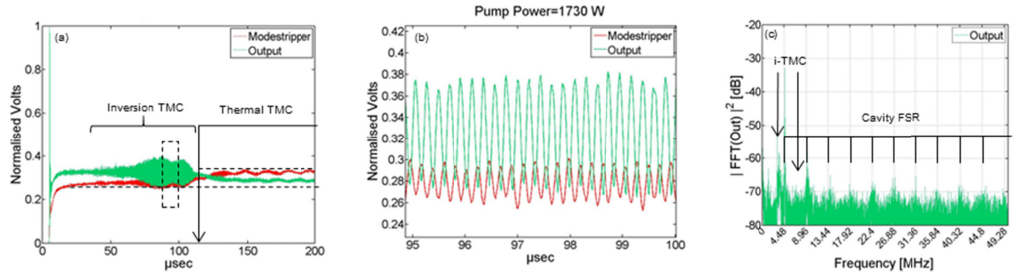

Fig. 9. Output power (PD#1-green) and CMS (PD#2-red) readings over (a) entire pump pulse duration (0-200μs), and (b) zoomed in the 95-100μs region (dotted square) and (c) FFT of output trace over 20-200μs period. The pump power is 1730W.

Optics EXPRESS

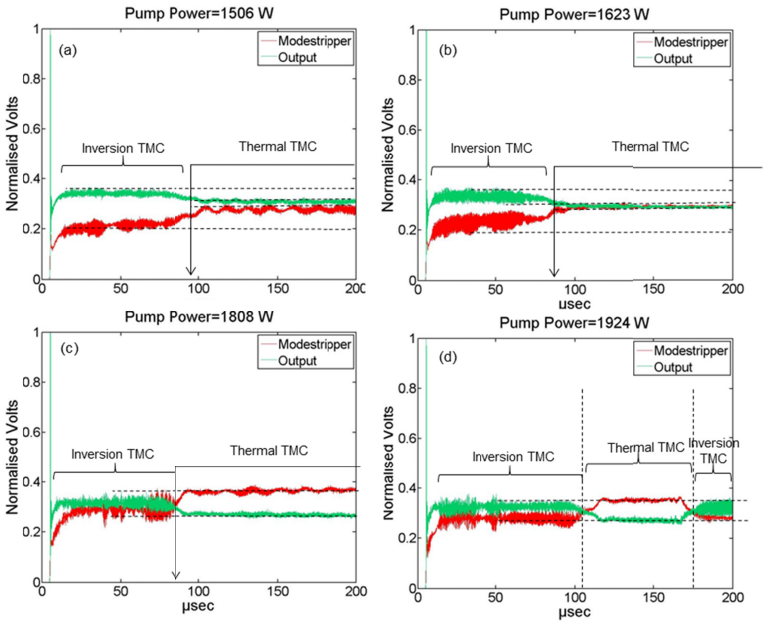

Fig. 10. Output power (PD#1-green) and HOM (PD#2-red) traces at pump powers of (a) 1506W, (b) 1623W, (c) 1808W and (d) 1924W.

Similar responses were observed at all power levels within zone#2. Figures 10(a) and 11(d) show the output power (PD#1-green) and HOM (PD#2-red) traces at different pump powers. It is shown that, after the pumps are turned-on, the first relaxation oscillation is followed by fast, inversion-related TMC (i-TMC) over a period of 80-100µs. The i-TMC period is always characterized by fast (MHz range) inter-modal power exchange around constant average levels. This period is interrupted by sudden onset of much slower (~50kHz) dynamics, in line with thermal diffusion time scales. Over this thermal TMC (t-TMC) period there is a marked change of the PD#1 and PD#2 average readings, indicating that thermal effects result in a strong intermodal power exchange. As Fig. 10(d) shows, the thermal TMC period was sometimes interrupted and reverted to a fast i-TMC regime, with the average FM and HOM powers returning to their initial values.

3.2.3 Instability zone#3

Instability zone#3 is characterized by a further decrease in output power slope and an associated larger slope of the HOM reading (PD#2), which indicates even stronger power exchange between FMC and HOMC. Figure 11 shows the results obtained with a pump power of 2303W (zone#2/zone#3 border) and 3000W. Figures 11(a) and 11(d) show that the first relaxation oscillations do not follow each other closely any more. Again, the fluctuations in the output power following the initial overshoots are believed to be due to the onset of backward SRS [2]. Figs. 11(b) and 11(e) are now characterized by much larger fast oscillations and stronger TMC due to inversion effects, throughout the pump pulse duration. The corresponding spectra in Figs. 11(c) and 11(f) show that the main TMC frequency has shifted to 4.45MHz (close to the cavity FSR) and 5.4MHz (exceeding the cavity FSR), respectively. At these power levels, within zone#3, the strong TMC provokes strong LMB, as evidenced again by the much increased levels of cavity FSR peaks. This strong coupling between transverse and longitudinal modes in the FMC and HOMC results in full chaotic operation.

Optics EXPRESS

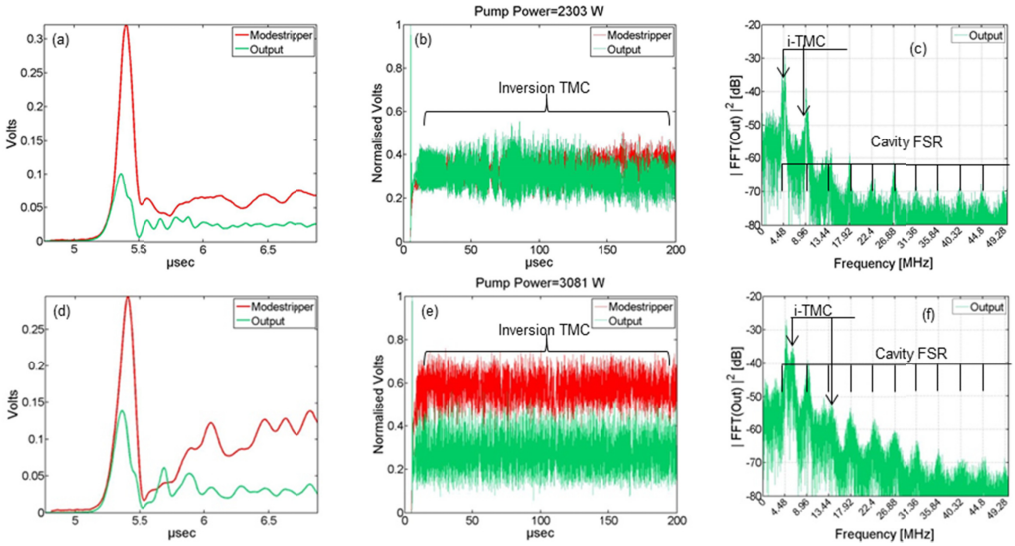

Fig. 11. Output power (PD#1-green) and CMS (PD#2-red) readings over (a),(d) relaxation oscillation (first 6.8µs), (b), (e) entire pump pulse duration (0-200µs), and (c), (f) FFT of output trace over 20-200µs period. The pump power is (a)-(c) 2303W, and (d)-(f) 3000W.

3.2.4 Instability map and route to chaos

Figure 12 shows the evolution of the fast TMC dynamics with pump power, in the frequency domain. Vertical lines on the frequency axis coincide with the fiber laser cavity FSR spacing due to LMB. Pump power axis incorporates 260 levels, ranging from 400W to 3000W in steps of 10W. The color scheme (z-axis - orthogonal to page) shows the absolute value of the FFT (in dB) of the output traces between 20 and 200µs. The three instability zones are also marked.

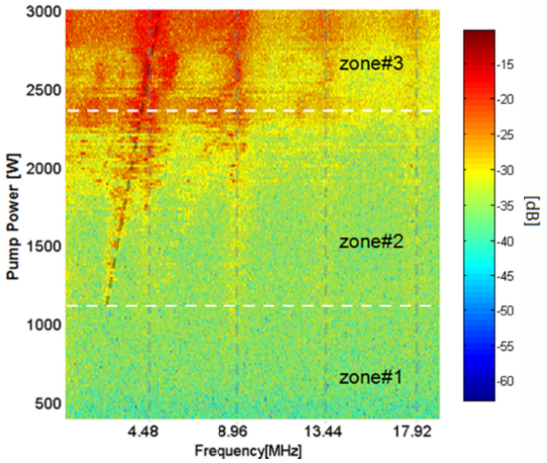

Fig. 12. Pulsed measurement, synoptic. X Axis: frequency of the FFT, Y Axis: Pump Power, Z axis (orthogonal to page): modulus of the FFT in dB.

Up to 1.2kW of pump power (zone#1), nothing is noticeable in the MHz range. In this zone, only thermally-induced TMC of fixed low frequency (~50kHz) has been observed (see Fig. 7). At a pump power of ~1.2kW (zone#2 bottom-end), a pronounced inversion-related TMC peak appears at ~2.5MHz. Further increase of pump power results in an quasi-linear increase of the dominant TMC frequency. At a pump power of ~2.4 kW (zone#2 top-end), the

Optics EXPRESS

TMC frequency becomes resonant with the cavity FSR frequencies. Above this power level (zone#3) TMC provokes LMB and the laser acquires a chaotic output characteristics, which amounts to multiple strong FSR peaks and in-between spectral filling. At 2.4 kW, the chaotic behavior is characterized by a broad RF spectrum, showing conspicuous excitation of frequencies up to ~13MHz. Within zone#3 above 2.4kW, the dominant TMC peak is larger than and no longer resonant with the first FSR peak. The sustained broad RF spectrum indicates persistent chaotic behavior.

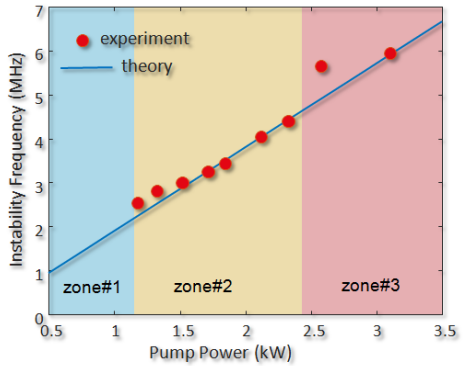

Fig. 13. Inversion TMC's frequency dependence on pump power – comparison with theory.

In Fig. 13, the variation of the dominant TMC frequency is compared with the population inversion related theoretical prediction (Eq. (9) in Appendix A). For the theoretical prediction, we have used parameters similar to the experimental values. The optical to optical conversion efficiency is ~55%, the pump wavelength is 950nm, the signal wavelength is 1070nm and the glass host was considered to be phosphosilicate. Theoretical and experimental results show a very good agreement. The quasi-linear dependence of the dominant TMC peak on the laser power further corroborates the dominant population inversion contribution to the observed TMC in zones#2 and #3.

4. Discussion - conclusions

In this work, CW and transient TMC in HPFL oscillators has been studied experimentally, by monitoring the dynamic power exchanges and characteristic frequencies of the transmitted FM and scattered HOMs of the fiber laser cavity, under CW and pulsed pumping. The FM and HOM power evolution indicates the presence of two competing effective laser cavities, which result in rich output dynamics and full chaotic operation.

As discussed in the introduction, TMI effects in high power amplifiers are attributed predominantly to thermal effects. However, in the case of high power oscillators, the current work shows that the observed TMC phenomena are due to combined and interleaved inversion- and thermally-related effects, with distinctively different characteristic frequencies and power dependencies.

The CW characterization obtained with slow detection shows the presence of TMC with envelopes on a slow seconds-timescale. Increasing the detection bandwidth by switching the oscilloscope impedance from high to low revealed the presence of superimposed high frequency (in the several MHz) content. Average values obtained from CW measurement are divided in three zones with progressively smaller output power efficiency.

In low-power zone#1, only slow power variations are observed. At the top-end of zone#1, a pronounced thermally-induced TMC is measured with characteristic frequencies in the ~50kHz range.

In zone#2, both thermal and inversion induced TMC coexist. The relative thermal and inversion related contributions to the observed TMC have been identified by monitoring the

associated characteristic instability frequencies, under pulsed pumping. It is shown that in the transient regime, both inversion and thermal effects contribute successively to the observed power instabilities. In most of the cases, the output power initial relaxation overshoot is followed by fast (in the MHz range) inversion-related power competition between FM and HOMs with null average power exchange. Thermal effects overtake after ~80-100μs, showing much slower dynamics (in the 10s of kHz range) and characterized by marked FM/HOM power exchange.

At the bottom-end of zone#2, inversion dominated TMC appears with characteristic frequencies ~2.5MHz (about half the cavity FSR). The instability characteristic frequency increases linearly with pump power until it matches the cavity FSR (first LMB) frequency at the top-end of zone#2. Further pump power increase into section#3 drives the HPFL into full chaotic behavior.

The co-existence and relative importance of the two effective cavities depends on the degree of HOM excitation at the SM-to-MM splices. Better matching between fibers and better quality splices reduce the competition between the two overlapping cavities and result in stable operation. Single fiber laser oscillators with more than 4kW stable output power have been recently demonstrated [37].

Appendix A: Inversion and thermal timescales in high power fibre laser transients.

Transients in optical fibre lasers and amplifiers, due to pump and/or signal changes, are characterized by specific time scales defined by the dominant optical effects. Although population inversion and thermal effects are intimately interlinked, their characteristic time scales can differ substantially, depending on the operating and boundary conditions [7,8], [35,38].

Thermal diffusion time scales

The temperature change distribution ΔT(r,φ,z;t) is given by the heat Eq. (1) [36]:

$$\frac{d\Delta T}{dt} - \alpha \nabla_T^2(\Delta T) = \frac{Q_T}{\rho_0 C_0} \tag{1}$$

where $\alpha = \kappa_0 / \rho_0 C_0$ is the glass thermal diffusivity, ρ_0, C_0, κ_0 are the glass density, specific heat capacity and thermal conductivity, respectively, and Q_T is the heat power density. Heat diffusion time scales are obtained by setting $Q_T = 0$ for t>0. Assuming a step-index fiber with R_1 and R_2 core and cladding radii, respectively, and simplified initial condition $\Delta T(r,\varphi,t) = \Delta T_0$ for $r<R_1$ and $t = 0$, the temperature variation with time is then given by [35]:

$$\Delta T(r,t) = \Delta T_0 \sum_{n=1}^{\infty} A_n J_0\left(\frac{\beta_n r}{\sqrt{\alpha}}\right) \exp(-\beta_n^2 \, t), (t \geq 0) \tag{2}$$

where β_n (n = 1,2,3,…) are obtained from the boundary condition of the 3rd kind (BC#3):

$$J_0(z_n) - (z_n / H) J_1(z_n) = 0; \qquad H = R_2 h_2^* / \kappa_2^* \tag{3}$$

where z_n are the roots of Eq. (3) and $\beta_n = z_n \sqrt{\alpha} / R_2$ and h_2^*, κ_2^* are the convection coefficient and thermal conductivity, respectively, of the surrounding cooling medium. The amplitude of the n^{th} thermal component is given by:

$$A_n = \int_0^{R_1} r' J_0\left(\beta_n r' / \sqrt{\alpha}\right) dr' \Big/ \int_0^{R_2} r' J_0^2\left(\beta_n r' / \sqrt{\alpha}\right) dr' \tag{4}$$

Optics EXPRESS

The diffusion time and the characteristic frequency of the n^{th} thermal component, on the other hand, are given by $\tau_n^{th} = \beta_n^{-2}$ and $f_n^{th} = \beta_n^2$, respectively. The case of large convection coefficient $\left(h_2^* \gg 1; H \to \infty\right)$ corresponds to the boundary condition of the 1st kind (BC#1), namely, $J_0(z_n) = 0$.

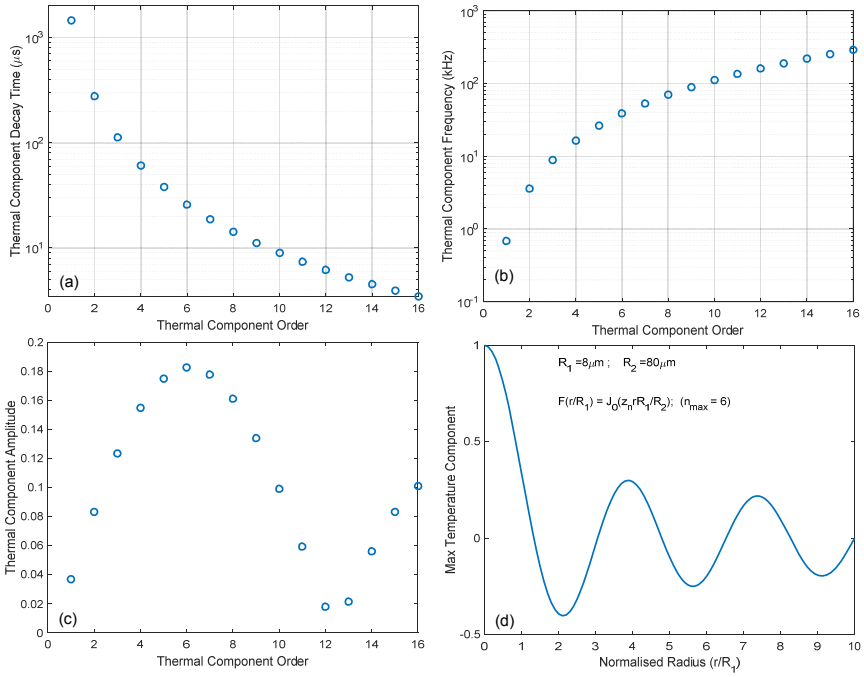

Fig. 14. (a) Diffusion time, (b) characteristic frequency and (c) amplitude of the n^{th} thermal component, for initial condition $\Delta T(r,\varphi,t) = \Delta T_0$ for $r<R_1$ and $t = 0$, and BC#1, (d) temperature variation of the maximum thermal component ($n = 6$); $R_1 = 8\mu m$ and $R_2 = 80\mu m$.

Figure 14 plots (a) the diffusion time (τ_n^{th}), 14(b) characteristic frequency (f_n^{th}) and 14(c) amplitude (A_n) of the n^{th} thermal component, for an initial condition $\Delta T(r,\varphi,t) = \Delta T_0$, for $r<R_1$ and $t = 0$, and BC#1. It is shown that the diffusion time (characteristic frequency) decreases (increases) monotonically with the order of the thermal component. This is due to the fact that thermal components of higher order show more and, therefore, sharper temperature variations along the fiber radius and, as a consequence, they diffuse faster. The amplitude of the thermal component, on the other hand, varies non-monotonically with order n and shows a maximum for the $n = 6$. The corresponding diffusion time and characteristic frequency is ~25μs and 40kHz, respectively. Figure 14(d) plots the temperature variation along the normalized fiber radius for the maximum thermal component ($n = 6$). For BC#1, the diffusion time of the n^{th} thermal component can be approximated by $\tau_n^{th} \approx R_2^2/(\alpha\pi^2 n^2)$.

Figure 15 plots (a) the diffusion time, and (b) the characteristic frequency of the maximum thermal component, as a function of the core radius. The initial condition is again $\Delta T(r,\varphi,t) = \Delta T_0$, for $r<R_1$ and $t = 0$, and BC#1 (blue line) and BC#3 (red line) are considered. The cladding/core ratio R_2/R_1 is 10. It is shown that the dominant diffusion time (frequency) increases (decreases) quasi-quadratically with the core radius.

Optics EXPRESS

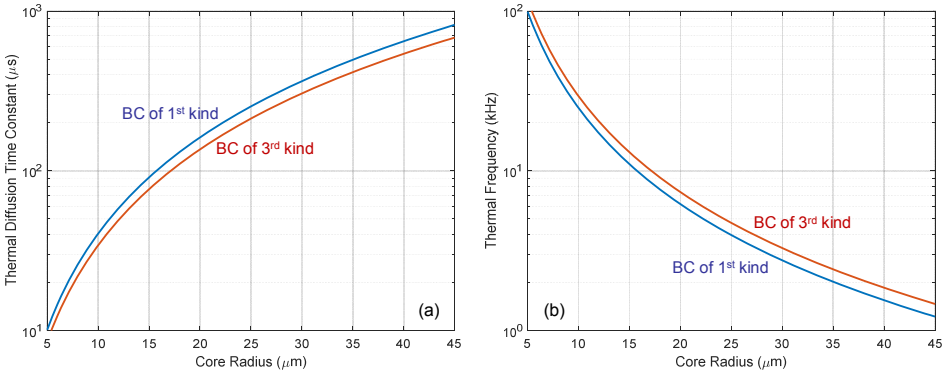

Fig. 15. (a) Diffusion time, (b) characteristic frequency of the maximum thermal component, as a function of the core radius. Initial condition $\Delta T(r,\varphi,t) = \Delta T_0$, for $r<R_1$ and $t = 0$, and BC#1 (blue line) and BC#3 (red line). Ratio $R_2 / R_1 = 10$.

Figure 15 also shows that the dominant thermal component diffusion time depends on the boundary conditions, with BC#3 having smaller diffusion times than BC#1. This is due to the fact that the dominant thermal components under BC#3 correspond to $n = 7$ and, therefore, have sharper temperature features (see Fig. 16) and, consequently, smaller diffusion times.

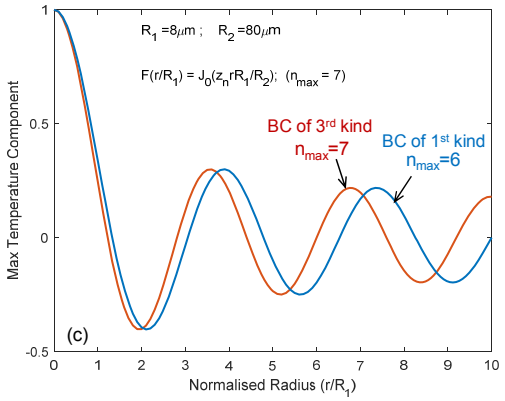

Fig. 16. Temperature variation of the maximum thermal component for BC1 (n = 6) and BC3 (n = 7). Initial condition $\Delta T(r,\varphi,t) = \Delta T_0$, for $r<R_1$ and $t = 0$, and BC#1 (blue line) and BC#3 (red line). $R_1 = 8\mu m$ and $R_2 = 80\mu m$.

It can be shown that the variation of the dominant diffusion time with core radius for BC#1 can be approximated by $\tau_{th} \approx R_{1eff}^2 / (2.405^2 \alpha)$. It should be mentioned that the usually quoted approximation of the timescale associated with thermal effects $\tau'_{th} \approx R_1^2 / \alpha$ [7,8,36] overestimates diffusion times by a factor of ~4.

Population inversion related time scales

Another mechanism that can induce index modulation and power exchange between modes is the inversion of the medium. The variation of the spatially averaged excited state population distribution N_2 is given by [7]:

$$\frac{dN_2}{dt} + \frac{N_2}{\tau_{eff}^{inv}} = \frac{N_0}{\tau}\left[\frac{\sigma_{ap}}{\sigma_{ap}+\sigma_{ep}}\left(\frac{I_p}{I_p^{sat}}\right) + \frac{\sigma_{as}}{\sigma_{as}+\sigma_{es}}\left(\frac{I_s}{I_s^{sat}}\right)\right] \quad (5)$$

Optics EXPRESS

where $I_s^{sat} = hv_s \big/ \left[\tau\left(\sigma_{as} + \sigma_{es}\right)\right]$ and $I_p^{sat} = hv_p \big/ \left[\tau\left(\sigma_{ap} + \sigma_{ep}\right)\right]$ are the signal and pump saturation intensities, respectively, τ is the upper-state population lifetime and τ_{eff}^{inv} is the corresponding effective lifetime given by:

$$\tau_{eff}^{inv} = \frac{\tau}{1 + I_p \big/ I_p^{sat} + I_s \big/ I_s^{sat}} \tag{6}$$

The signal and pump intensities are approximated by $I_s = P_s \big/ \left(\pi R_1^2\right)$ and $I_p = P_p \big/ \left(\pi R_2^2\right)$, respectively. For a fixed pump intensity I_p and a change of signal intensity from I_{s1} to I_{s2} at t = 0, the upper-lever population varies as:

$$N_2(t) = N_2^{ss}(I_{s2}; I_p) + \left[N_2^{ss}(I_{s1}; I_p) - N_2^{ss}(I_{s2}; I_p)\right] \exp\left(-t \big/ \tau_{eff}^{inv}\right); \ (t \geq 0) \tag{7}$$

where $N_2^{ss}(I_{s1}; I_p)$, $N_2^{ss}(I_{s2}; I_p)$ are the corresponding steady-state upper-state populations given by:

$$N_2^{ss}(I_s; I_p) = N_0 \left\{ \left[\frac{\sigma_{ap}}{\sigma_{ap} + \sigma_{ep}} \left(\frac{I_p}{I_p^{sat}} \right) + \frac{\sigma_{as}}{\sigma_{as} + \sigma_{es}} \left(\frac{I_s}{I_s^{sat}} \right) \right] \Bigg/ \left(1 + \frac{I_p}{I_p^{sat}} + \frac{I_s}{I_s^{sat}} \right) \right\} \tag{8}$$

The associated characteristic frequencies are given by

$$f_{eff}^{inv} = \frac{1}{\tau_{eff}^{inv}} = \frac{1}{\tau} \left(1 + \frac{I_p}{I_p^{sat}} + \frac{I_s}{I_s^{sat}} \right) \tag{9}$$

From Eqs. (6) and (9), it is deduced that the characteristic time scales and frequencies depend on core/cladding radii, as well as, the pump and signal powers. Figures 17(a) and 17(b) plot the effective upper-level decay time, and corresponding effective frequency, respectively, as a function of signal power, for different core diameters. The optical-to-optical conversion efficiency is assumed 80%, and the cladding/core ratio R_2/R_1 = 10. The signal and pump wavelengths are λ_s = 1070nm and λ_p = 915nm, respectively, and the fiber core is considered to be of phosphosilicate composition.

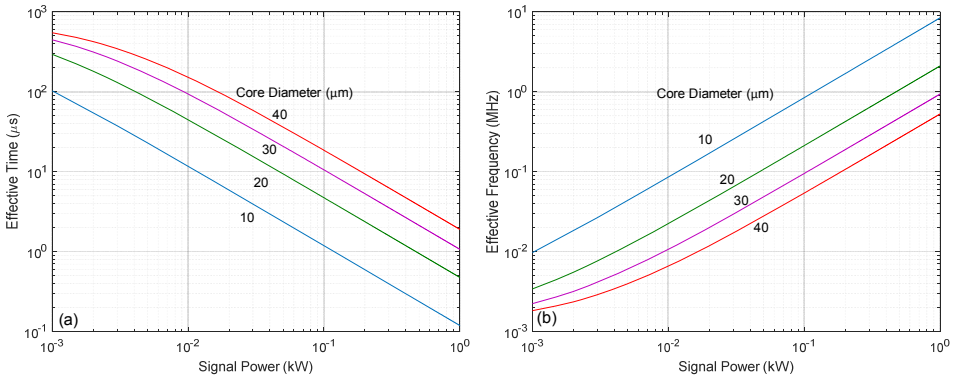

Fig. 17. (a) Effective upper-level decay time, and (b) corresponding effective frequency as a function signal power, for different core radii. Optical-to-optical conversion efficiency = 80%, ratio R_2/R_1 = 10, λ_s = 1070nm, λ_p = 915nm, phosphosilicate fiber.

Optics EXPRESS

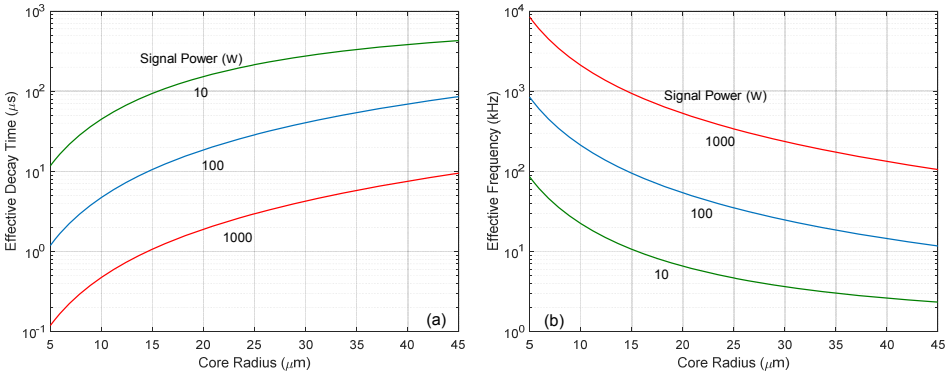

Fig. 18. (a) Effective upper-level decay time, and (b) corresponding effective frequency as a function core radius, for different signal powers. Optical-to-optical conversion efficiency = 80%, ratio $R_2/R_1 = 10$, $\lambda_s = 1070$nm, $\lambda_p = 915$nm, phosphosilicate fiber.

Figures 18(a) and 18(b) plot the effective upper-level decay time, and corresponding effective frequency, respectively, as a function of core radius, for different signal powers. The other parameters are as in Fig. 17.

In Fig. 17(b) it is shown that, in inversion dominated dynamics for $I_s / I_s^{sat} > 1$ and fixed core/cladding radii, the effective frequency increases linearly with the signal power. Figure 18(b), on the other hand, shows that for fixed power the effective frequency is inversely proportional to the core area, in a similar manner to thermally-induced effects (see Fig. 15(b)). Comparing Figs. 15(b) and 18(b), however, it is becomes apparent that thermally-induced transients show similar effective frequencies (~1-100kHz) only in the case of low signal power inversion-related dynamics (i.e. signal power ~10W). As the signal power is increased to kW level, the inversion-related frequencies increase to a 100kHz to 10s-of-MHz regime, while thermally-dominated transients are largely power independent.

At this point, it should be emphasized that the signal power dependence of the characteristic frequencies of the induced transients and their range of variation can be used as an indicator of the dominant (inversion or thermal) contributor to the observed power transients and instabilities in high power fiber lasers and amplifiers.

All data supporting this study are openly available from the University of Southampton repository [39].

Funding

Engineering and Physical Sciences Research Council (EPSRC) (EP/P027644/1)

Acknowledgments

Royal Academy of Engineering Research Chairs and Senior Research Fellowships Scheme.

References

1. T. Eidam, C. Wirth, C. Jauregui, F. Stutzki, F. Jansen, H.-J. Otto, O. Schmidt, T. Schreiber, J. Limpert, and A. Tünnermann, "Experimental observations of the threshold-like onset of mode instabilities in high power fiber amplifiers," Opt. Express **19**(14), 13218–13224 (2011).
2. M. N. Zervas, "Power Scalability in High Power Fibre Amplifiers" in 2017 European Conference on Lasers and Electro-Optics and European Quantum Electronics Conference (Optical Society of America, 2017), p. CJ_6_1.
3. M. N. Zervas, "Power scaling limits in high power fiber amplifiers due to transverse mode instability, thermal lensing, and fiber mechanical reliability," Proc. SPIE **10512**, 1051205 (2018).
4. C. Jauregui, T. Eidam, H.-J. Otto, F. Stutzki, F. Jansen, J. Limpert, and A. Tünnermann, "Physical origin of mode instabilities in high-power fiber laser systems," Opt. Express **20**(12), 12912–12925 (2012).
5. K. R. Hansen, T. T. Alkeskjold, J. Broeng, and J. Lægsgaard, "Theoretical analysis of mode instability in high-power fiber amplifiers," Opt. Express **21**(2), 1944–1971 (2013).

Optics EXPRESS

6. L. Dong, "Stimulated thermal Rayleigh scattering in optical fibers," Opt. Express **21**(3), 2642–2656 (2013).
7. A. V. Smith and J. J. Smith, "Mode instability in high power fiber amplifiers," Opt. Express **19**(11), 10180–10192 (2011).
8. H.-J. Otto, F. Stutzki, F. Jansen, T. Eidam, C. Jauregui, J. Limpert, and A. Tünnermann, "Temporal dynamics of mode instabilities in high-power fiber lasers and amplifiers," Opt. Express **20**(14), 15710–15722 (2012).
9. B. Ward, C. Robin, and I. Dajani, "Origin of thermal modal instabilities in large mode area fiber amplifiers," Opt. Express **20**(10), 11407–11422 (2012).
10. S. Naderi, I. Dajani, T. Madden, and C. Robin, "Investigations of modal instabilities in fiber amplifiers through detailed numerical simulations," Opt. Express **21**(13), 16111–16129 (2013).
11. M. Karow, H. Tünnermann, J. Neumann, D. Kracht, and P. Wessels, "Beam quality degradation of a single-frequency Yb-doped photonic crystal fiber amplifier with low mode instability threshold power," Opt. Lett. **37**(20), 4242–4244 (2012).
12. D. Engin, J. Burton, I. Darab, F. Kimpel, and S. Gupta, "Yb-fiber-MOPA based high energy and average power uplink laser beacon for deep space communication operating under Nested PPM format," Proc. SPIE **9466**, 94660V (2015).
13. K. Brar, M. Savage-Leuchs, J. Henrie, S. Courtney, C. Dilley, R. Afzal, and E. Honea, ""Threshold power and fiber degradation induced modal instabilities in high-power fiber amplifiers based on large mode area fibers," in Fiber Lasers XI: Technology, Systems, and Applications," Proc. SPIE **8961**, 89611R (2014).
14. R. Tao, P. Ma, X. Wang, P. Zhou, and Z. Liu, "Mitigating of modal instabilities in linearly-polarized fiber amplifiers by shifting pump wavelength," J. Opt. **17**(4), 045504 (2015).
15. P. Ma, R. Tao, R. Su, X. Wang, P. Zhou, and Z. Liu, "1.89 kW all-fiberized and polarization-maintained amplifiers with narrow linewidth and near-diffraction-limited beam quality," Opt. Express **24**(4), 4187–4195 (2016).
16. M. Kuznetsov, O. Vershinin, V. Tyrtyshnyy, and O. Antipov, "Low-threshold mode instability in Yb3+-doped few-mode fiber amplifiers," Opt. Express **22**(24), 29714–29725 (2014).
17. O. Antipov, M. Kuznetsov, D. Alekseev, and V. Tyrtyshnyy, "Influence of a backward reflection on low-threshold mode instability in Yb^{3+}-doped few-mode fiber amplifiers," Opt. Express **24**(13), 14871–14879 (2016).
18. B. G. Ward, "Modeling of transient modal instability in fiber amplifiers," Opt. Express **21**(10), 12053–12067 (2013).
19. M. N. Zervas, "TMI Threshold in High Power Fiber Amplifiers," in Advanced Photonics 2016 (IPR, NOMA, Sensors, Networks, SPPCom, SOF), OSA Technical Digest (Online) (Optical Society of America, 2016), p. SoW2H.2.
20. M. N. Zervas, "Transverse mode instability analysis in fiber amplifiers" Proc. SPIE **10083**, 100830M (2017).
21. G. P. Agrawal, *Nonlinear Fiber Optics,* 5th ed. (Academic Press, 2012), Chap. 5.
22. G. H. M. van Tartwijk and G. P. Agrawal, "Maxwell–Bloch dynamics and modulation instabilities in fiber lasers and amplifiers," J. Opt. Soc. Am. B **14**(10), 2618–2627 (1997).
23. K. Hejaz, A. Norouzey, R. Poozesh, A. Heidariazar, A. Roohforouz, R. Rezaei Nasirabad, N. Tabatabaei Jafari, A. Hamedani Golshan, A. Babazadeh, and M. Lafouti, "Controlling mode instability in a 500 W ytterbium-doped fiber laser," Laser Phys. **24**(2), 025102 (2014).
24. B. Yang, H. Zhang, C. Shi, X. Wang, P. Zhou, X. Xu, J. Chen, Z. Liu, and Q. Lu, "Mitigating transverse mode instability in all-fiber laser oscillator and scaling power up to 2.5 kW employing bidirectional-pump scheme," Opt. Express **24**(24), 27828–27835 (2016).
25. M.-A. Malleville, R. Dauliat, A. Benoît, B. Leconte, D. Darwich, R. D. Jeu, R. Jamier, K. Schuster, and P. Roy, "Experimental study of the mode instability onset threshold in high-power FA-LPF lasers," Opt. Lett. **42**(24), 5230–5233 (2017).
26. B. Yang, H. Zhang, C. Shi, R. Tao, R. Su, P. Ma, X. Wang, P. Zhou, X. Xu, and Q. Lu, "3.05 kW monolithic fiber laser oscillator with simultaneous optimizations of stimulated Raman scattering and transverse mode instability," J. Opt. **20**(2), 025802 (2018).
27. J. Lægsgaard, "Static thermo-optic instability in double-pass fiber amplifiers," Opt. Express **24**(12), 13429–13443 (2016).
28. C. Stihler, H.-J. Otto, C. Jauregui, J. Limpert, and A. Tünnermann, "Experimental investigation of transverse mode instabilities in a double-pass Yb-doped rod-type fiber amplifier," Proc. SPIE **10083**, 100830R (2017).
29. D. Alekseev, V. Tyrtyshnyy, M. Kuznetsov, and O. Antipov, "Transverse-Mode Instability in High-Gain Few-Mode Yb3+-Doped Fiber Amplifiers With a 10-μm Core Diameter With or Without Backward Reflection," IEEE J. Sel. Top. Quantum Electron. **24**(3), 1–8 (2018).
30. N. Haarlammert, O. de Vries, A. Liem, A. Kliner, T. Peschel, T. Schreiber, R. Eberhardt, and A. Tünnermann, "Build up and decay of mode instability in a high power fiber amplifier," Opt. Express **20**(12), 13274–13283 (2012).
31. C. Jauregui, C. Stihler, A. Tünnermann, and J. Limpert, "Pump-modulation-induced beam stabilization in high-power fiber laser systems above the mode instability threshold," Opt. Express **26**(8), p.10691 (2018).
32. C. Stihler, C. Jauregui, A. Tünnermann, and J. Limpert, "Modal energy transfer by thermally induced refractive index gratings in Yb-doped fibers," Light Sci. Appl. **7**(1), 59 (2018).
33. A. B. Grudinin, D. N. Payne, P. W. Turner, J. Nilsson, M. N. Zervas, M. Ibsen, and M. K. Durkin, "Multi-fibre arrangements for high power fibre lasers and amplifiers", U.S. patent 6,826,335 (April 28, 2000).

Optics EXPRESS

34. M. N. Zervas, A. Marshall, and J. Kim, "Effective absorption in cladding-pumped fibers," Proc. SPIE **7914**, 79141T (2011).
35. M. N. Ozisik, *Heat Conduction* (J. Wiley, 1993)
36. R. W. Boyd, *Nonlinear Optics* (Academic Press, 2008), Chap. 4.
37. K. Shima, S. Ikoma, K. Uchiyama, Y. Takubo, M. Kashiwagi, and D. Tanaka, "5-kW single stage all-fiber Yb-doped single-mode fiber laser for materials processing," Proc. SPIE **10512**, 105120C (2018).
38. H. S. Carslaw and J. C. Jaeger, *Conduction of Heat in Solids,* 2nd ed. (Clarendon Press, 1959).
39. All data supporting this study are openly available from the University of Southampton repository at: https://eprints.soton.ac.uk/426357